Paper:

Impact of Climate Change on Flood Hazard at Airports on Pacific Islands: A Case Study of Faleolo International Airport, Samoa

Lianhui Wu*, **Kenji Taniguchi****, **and Yoshimitsu Tajima***,†

*Department of Civil Engineering, The University of Tokyo
7-3-1 Hongo, Bunkyo-ku, Tokyo 113-8656, Japan
†Corresponding author, E-mail: yoshitaji@coastal.t.u-tokyo.ac.jp
**Faculty of Geosciences and Civil Engineering, Kanazawa University, Ishikawa, Japan
[Received October 6, 2020; accepted December 31, 2020]

Climate change is believed to have increased the intensity and frequency of heavy rainfall, and also to have caused sea level rises over this century and beyond. There is widespread concern that small-island nations are particularly vulnerable to increasing risk of inland flood due to such climate change. Understanding the impact of climate change on flood hazard is of great importance for these countries for the development of better protection and adaptation strategies. This study conducted a case study focusing on the impact of climate change on flood hazard at Faleolo International Airport (FIA), Samoa. FIA is a typical small islands airport, located on the lowland along the coast fronted by a fringing reef. Annual maximum daily rainfalls for different return periods were first estimated for the present and future climate around FIA. The estimated rainfalls were input as the forcing of a two-dimensional flood inundation model to investigate the flooding behavior and effectiveness of probable drainage systems. Results showed that a part of the runway can be inundated under heavy rainfall. Construction of drainage pipes significantly contributes to reducing the flood hazard level. Sensitivity analysis showed that the astronomical tide level has relatively little influence on the performance of the drainage system, while the combination of sea level rise and the sea level anomaly induced by stormy waves on the fringing reef could have non-negligible impacts on the drainage system. Location of the drainage pipe is also important to effectively mitigate flooding. The time-concentration of torrential rainfall may also significantly impact the overall performance of the drainage system.

Keywords: flood hazard, climate change, drainage strategy, flooding mitigation, sensitivity analysis

1. Introduction

Global warming will most likely continue over this century and beyond, amplifying existing risks and possibly creating new risks to natural and manmade systems [1]. Small-island countries may be more vulnerable to the impact of global warming [2]. These small islands are facing such challenges as sea level rise, coastal erosion, increased incidence of drought, coral bleaching, storm surges, and flooding [3]. Among these, sea level rise has received more attention than the others because it is a common problem for island nations. The rising sea level will lead to more significant coastal inundation, erosion, and saltwater penetration [4–6]. On the other hand, the number of studies related to flooding induced by heavy rainfall is limited, even though flooding in the lowlands of these islands should be greatly aggravated by both increased intensive rainfall and sea level rise.

Global warming leads to greater evaporation and therefore more intense precipitation in some regions, and these events have been widely observed [7]. The current drainage system may not be sufficient to accommodate such increased precipitation, resulting in higher flood risk. In addition, the frequency, duration, and intensity of tropical cyclones have all increased since the early 1980s [8, 9]. These cyclones may also place higher stress on the drainage system to cope with the flooding.

Among developing island nations, the lack of essential infrastructure for draining heavy precipitation will amplify the risk of inland flooding. Practical measures will be needed for developing small-island countries to adapt to the increasing risk of inland flooding due to climate change. A cost-effective drainage strategy is necessary to protect flood-prone areas because the financial budget is usually limited in these island countries. As a case study, this paper aims to investigate the flooding hazard in Faleolo International Airport (FIA), Samoa, and to explore the efficient drainage strategy under future rainfall scenarios.

Fig. 1. Satellite image of the target site, Faleolo International Airport (rectangle) in Samoa.

2. Study Area

This study focuses on FIA, which is located 40 km west of Apia, the capital of Samoa (**Fig. 1**). FIA accommodates the majority of international flights in and out of Samoa. FIA is located on the north coast of the island and has a 3.5 km-long runway parallel to the shoreline within a distance of 50 m from the sea, fronted by a fringing reef (**Fig. 2**). The main runway is paved, connecting to the apron by two taxiways. The study area is relatively flat and low lying, and is a typical airport on Pacific islands. The airport is surrounded by coastal tropical forest. This region has a characteristic climate with abundant rainfall and high humidity. Therefore, the moisture of the soil surrounding the airport is relatively high. The amount of surface soil absorption is not great, and thus high surface runoff is expected to propagate to the area of the main runway, located in the lowest part of the site. Efficient drainage infrastructures have not been constructed in this region, and thus insufficient drainage may amplify the flood under stormy conditions. Since there is no seawall constructed along the shoreline, rainwater on the seaside of the runway may be directly drained on the ground surface. The surface water on the landside of the runway, however, might not drain because the paved runway is elevated, and water may thus remain for a long time because of the relatively small infiltration rate of the ground surface. Moreover, a part of the runway and taxiways may be inundated when the rainfall is severe. In fact, FIA has been inundated several times in the past. **Fig. 4** shows the target site after a heavy rainfall event in February 2018. Efficient drainage strategy is therefore crucial to mitigate the flood risk at FIA.

3. Estimation of Future Rainfall

To evaluate the possible flood inundation risk in the future, estimation of suitable forcing is important. Future projections from the general circulation model (GCM) could give possible variations under the global warming condition. However, spatial resolutions of GCMs are too coarse to serve as forcing in inundation simulations for a specific basin or around a facility. In this study, high-spatial resolution future rainfall information (HRFR) was estimated using satellite-based rainfall data and future projections by GCMs. Annual maximum daily rainfalls for different return periods were then estimated for present and future climate. Detailed procedures of rainfall estimation are described in this section.

3.1. Data

There are not sufficient observation data in Samoa to investigate the climatological characteristics of rainfall. Global Satellite Mapping of Precipitation (GSMaP) is the combined rainfall product of multiple satellite observation data [10]. In the GSMaP product, hourly rain rate is estimated by observation data from space-borne precipitation radar onboard Tropical Rainfall Measuring Mission (TRMM) and the main satellite of Global Precipitation Measurement (GPM). The GSMaP product is available from March 2000 to the near real time. The temporal and spatial resolution of GSMaP product is 1 hour and 0.1 degree, respectively.

Future variations of rainfall characteristics are investigated from the products of global warming experiments by GCMs in the 5th phase of the Climate Model Intercomparison Project (CMIP5) [11]. There are several greenhouse gas concentration scenarios (i.e., representative concentration pathways: RCPs) in the CMIP5 experiments. In this study, 3-hourly rainfall products under the historical and the RCP8.5 scenarios were used to generate HRFR. Historical experiments in CMIP5 are reproductive simulations from the mid-19th century to the beginning of 21st century. In the RCP8.5 scenario, the radiative forcing of the Earth in 2100 is greater than the preindustrial level by 8.5 W/m^2. Results for 20 years from the historical and the RCP8.5 experiments (i.e., 1986–2005 and 2081–2100, respectively) were used to investigate differences in rainfall characteristics between the current and future climate conditions. The applicability of 18 GCMs was examined in this study (**Table 1**).

3.2. Extraction of Rainfall

To prepare forcing for the inundation simulations around FIA, rainfall data are extracted for the area including Upolu Island. For GSMaP, spatial mean rainfall values are extracted for the 1×1 degree area including 172.45W–171.45W, 13.25S–14.25S for the target period from March 2000 to December 2019. GCM output is the subset for one grid including Upolu Island. The target period for the historical and RCP8.5 scenario is 1986–2005 and 2081–2100, respectively.

Based on the 3-hourly GCMs rainfall, daily rainfalls were calculated for each day, and annual maximum daily rainfalls ($Rd_{\max}$) were compared between GSMaP and the historical output of CMIP5 products for the extracted 20 years. A boxplot of the 20-year $Rd_{\max}$ is shown in **Fig. 5**. In many GCMs, mean and maximum $Rd_{\max}$ are smaller than GSMaP around Upolu Island.

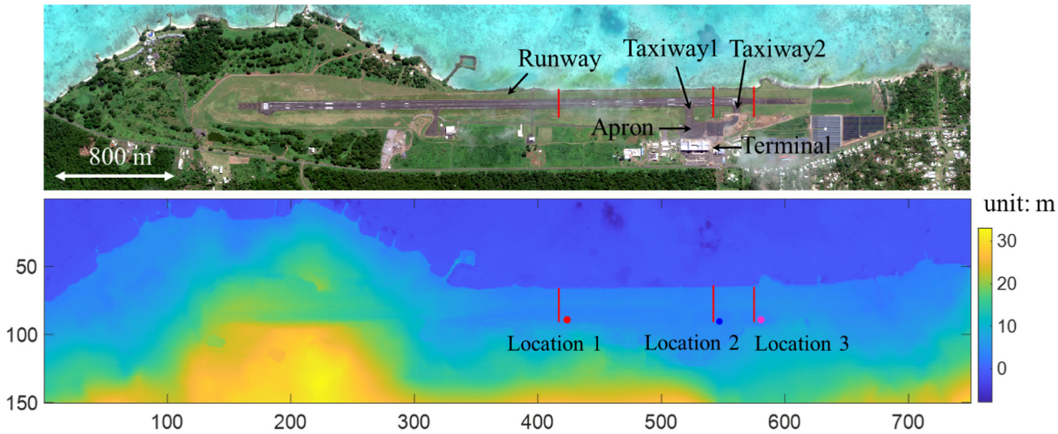

Fig. 2. Map of the study area (upper panel), digital elevation map of the study area with a grid size of 8 m (lower panel). Designed drainage pipes are indicated by solid red lines. Dots are positioned to show the time series of inundation depth in **Fig. 3**.

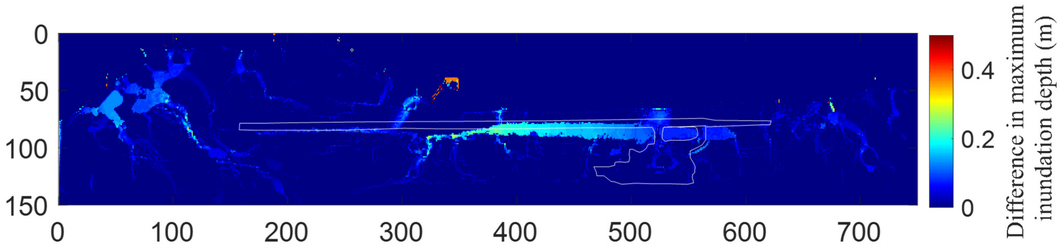

Fig. 3. Difference in MID between Case 15 and Case 6.

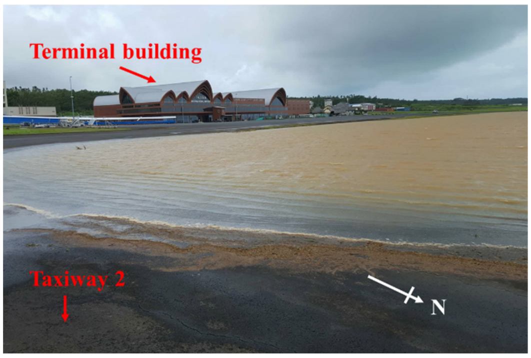

Fig. 4. Picture of the target site after the heavy rainfall event in February 2018.

3.3. Expansion of Rainfall for Future Climate

Based on a downscaling method using the cumulative distribution function [12, 13], HRFR is generated for Upolu Island. **Fig. 6** shows an example of the top 10,000 3-hourly mean rain rates (mm/h) by GCM. In RCP8.5, the upper-level rain rate is greater than the historical rate. On the other hand, there is little difference in the weak rain rate between RCP8.5 and the historical run. Therefore, the modification rate is estimated for the top 10,000 rain rates from GCM output. The modification rate is defined as follow:

$$M_{i,A} = \frac{RR_{F,i,A}}{RR_{P,i,A}}. \quad \text{(1)}$$

Here, $M_{i,A}$ is the modification rate for the i-th rank rain rate for GCM A. $RR_{F,i,A}$ and $RR_{P,i,A}$ are the i-th rank rain rate for future and present climate, respectively. Then, GSMaP rain rate is modified as follow:

$$HRFR_{i,A} = RR_{GSMaP,i} \times M_{i,A}. \quad \text{(2)}$$

$HRFR_{i,A}$ and $RR_{GSMaP,i}$ are the i-th rank modified high resolution future rain rate using GCM A and the i-th rank GSMaP rain rate, respectively. **Fig. 7** is a schematic view of the modification of GSMaP rain rate. Based on the modified rain rate, annual maximum daily rainfall was calculated.

3.4. Estimation of the Maximum Daily Rainfall for Different Return Periods

Figure 8 is a boxplot for 20-year $Rd_{\max}$ derived from HRFR. Though the original $Rd_{\max}$ were quite different from GSMaP in some GCM results (**Fig. 5**), $Rd_{\max}$ by HRFR seems reasonable overall. To examine the appropriateness of HRFR, Standard Least Square Criteria (SLSC) were calculated for multiple probability distribution models based on 20-year $Rd_{\max}$ data by GSMaP and HRFR. **Table 2** shows the results for SLSC. Statistical values match the probability distribution model when SLSC < 0.03. The exponential distribution (Exp) and log-normal distribution (LN3Q) show better results. Considering $Rd_{\max}$ of the historical simulation (**Fig. 5**), HRFR based on MRI-CGCM3 was used to estimate $Rd_{\max}$ for different return periods.

Table 1. CMIP5 models used in this study.

Model ID	Institute
ACCESS1-0	CSIRO, Bureau of Meteorology, Australia
ACCESS1-3	
CMCC-CM	Centro Euro-Mediterraneo per i Cambiamenti Climatici, Italy
CNRM-CM5	Centre National de Recherches Météorologiques, France
FGOALS-g2	State Key Laboratory of Numerical Modeling for Atmospheric Sciences and Geophysical Fluid Dynamics, China
FGOALS-s2	
GFDL-CM3	National Oceanic and Atmospheric Administration/Geophysical Fluid Dynamics Laboratory, USA
GFDL-ESM2G	
GFDL-ESM2M	
HadGEM2-ES	UKMO Hadley Centre, UK
INM-CM4	Institute of Numerical Mathematics, Russia
IPSL-CM5A-LR	L'Institut Pierre-Simon Laplace, France
IPSL-CM5A-MR	
MIROC5	Atmosphere and Ocean Research Institute (The University of Tokyo), National Institute for Environmental Studies, Japan Agency for Marine-Earth Science and Technology, Japan
MIROC-ESM	
MIROC-ESM-CHEM	
MRI-CGCM3	Meteorological Research Institute, Japan
MRI-ESM1	

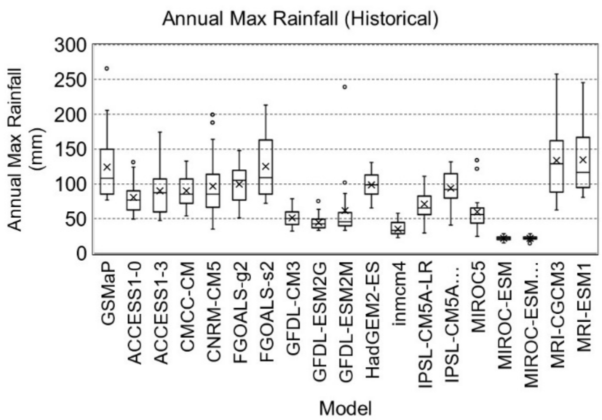

Fig. 5. Boxplot of 20-year annual maximum daily rainfalls for GSMaP and the historical experiment for each GCM.

Table 3 shows Rd_{max} estimated for some return periods in present and future climate. As the input for inundation simulations, GSMaP products for the heavy rainfall events in April 2016 were expanded to be the target Rd_{max} shown in **Table 3**.

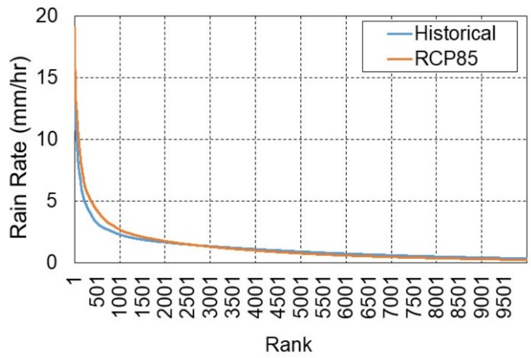

Fig. 6. Top 10,000 3-hourly mean rain rates (mm/h) for historical and RCP8.5 experiments. Results are shown for MRI-CGCM3.

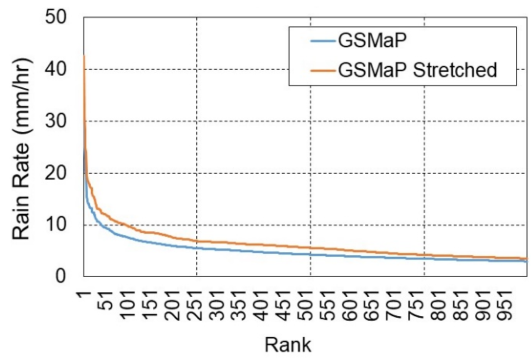

Fig. 7. Example of stretched GSMaP rain rates (HRFR) for top 1,000 3-hourly mean rain rates (mm/h).

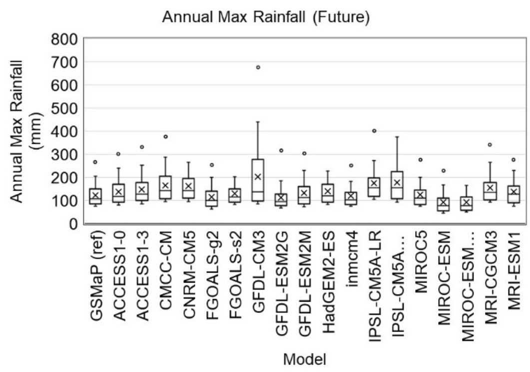

Fig. 8. Boxplot of 20-year annual maximum daily rainfall for GSMaP and HRFR of each GCM.

4. Inland Flooding Behaviors Under Future Rainfall

4.1. Inland Flooding Model

Based on the estimated daily rainfall probability, flooding behavior is evaluated by the two-dimensional (2D) overland flow model. The computational area is shown in **Fig. 2**. Topography data are obtained from the satellite-based product, AW3D Enhanced [14], with spatial resolution of 2 m. The computational area was determined

Table 2. SLSC for different probability distribution models. SLSC < 0.03 are indicated in bold font.

Source/Model ID	**SLSC**					
	Exp	**Gumbel**	**SQRTET**	**GEV**	**LogP3**	**LN3Q**
GSMaP	**0.026**	0.051	0.063	0.035	0.033	0.033
ACCESS1-0	**0.028**	0.051	0.065	0.037	0.034	**0.03**
ACCESS1-3	**0.027**	0.052	0.064	0.035	0.032	**0.03**
CMCC-CM	**0.027**	0.053	0.065	0.036	0.033	**0.03**
CNRM-CM5	**0.029**	0.051	0.059	0.034	0.032	**0.03**
FGOALS-g2	**0.027**	0.046	0.055	0.033	0.033	0.031
FGOALS-s2	0.033	0.049	0.061	0.04	0.038	0.037
GFDL-CM3	0.049	0.082	0.104	0.052	0.043	0.039
GFDL-ESM2G	0.062	0.092	0.104	0.035	0.031	**0.03**
GFDL-ESM2M	**0.03**	0.053	0.063	0.038	0.035	0.033
HadGEM2-ES	**0.025**	0.046	0.058	0.035	0.033	0.033
INM-CM4	0.034	0.055	0.067	0.038	0.036	0.036
IPSL-CM5A-LR	0.034	0.057	0.063	0.034	0.032	0.032
IPSL-CM5A-MR	0.036	0.044	0.052	0.041	0.04	0.041
MIROC5	**0.025**	0.048	0.056	0.032	0.031	0.032
MIROC-ESM	**0.027**	0.052	0.06	0.036	0.034	0.035
MIROC-ESM-CHEM	**0.021**	0.049	0.059	0.033	0.031	0.032
MRI-CGCM3	**0.027**	0.05	0.059	0.035	0.033	0.036
MRI-ESM1	0.031	0.037	0.043	0.034	0.039	0.039

*Exp: Exponential distribution, Gumbel: Gumbel distribution, SQRTET: Square-root exponential type maximum distribution, GEV: Generalized extreme value distribution, LogP3: Log-Pearson Type III distribution, LN3Q: Log-normal distribution.

Table 3. Annual maximum daily rainfalls for different return periods and designed rainfall scenarios for the inland flooding model.

Case No.	Climate pattern	Return period [year]	Daily rainfall [mm]	Rainfall duration [h]	Rainfall intensity [mm/h]
1	Present	25	245.8	6	40.96
2	Present	50	283.8	6	47.30
3	Present	75	306.0	6	51.00
4	Present	100	321.8	6	53.63
5	Present	125	334.0	6	55.66
6	Present	25	245.8	12	20.48
7	Present	50	283.8	12	23.65
8	Present	75	306.0	12	25.50
9	Present	100	321.8	12	26.82
10	Present	125	334.0	12	27.83
11	Future	25	316.6	6	52.77
12	Future	50	366.6	6	61.10
13	Future	75	395.8	6	65.97
14	Future	100	416.6	6	69.43
15	Future	125	432.7	6	72.12
16	Future	25	316.6	12	26.38
17	Future	50	366.6	12	30.55
18	Future	75	395.8	12	32.98
19	Future	100	416.6	12	34.71
20	Future	125	432.7	12	36.06

by a wide-area simulation conducted previously to ensure that the neighboring surface runoff routing does not affect the target area. The horizontal grid size is uniformly set to 8 m in both east-west (x-) and north-south (y-) directions to reduce the computational cost. There are 112,500 grids in the computation domain, covering a total area of 7.2 km^2. The overland flow is computed by the 2D Shallow Water equations, which represent the depth-integrated mass and momentum conservations,

$$\frac{\partial S}{\partial t} + \frac{\partial M}{\partial x} + \frac{\partial N}{\partial y} = R, \quad \ldots\ldots\ldots \quad (3)$$

$$\frac{\partial M}{\partial t} + \frac{\partial}{\partial x}\left(\frac{M^2}{D}\right) + \frac{\partial}{\partial y}\left(\frac{MN}{D}\right) + gD\frac{\partial S}{\partial x} + \frac{gn^2}{D^{\frac{7}{3}}}M\sqrt{M^2+N^2} = 0, \quad \ldots\ldots \quad (4)$$

$$\frac{\partial N}{\partial t} + \frac{\partial}{\partial y}\left(\frac{N^2}{D}\right) + \frac{\partial}{\partial x}\left(\frac{MN}{D}\right) + gD\frac{\partial S}{\partial y} + \frac{gn^2}{D^{\frac{7}{3}}}N\sqrt{M^2+N^2} = 0, \quad \ldots\ldots\ldots \quad (5)$$

where S is the water level on the land; t is time; M and N are the flow discharge per unit width in the x- and y-directions, respectively; R is the effective rainfall intensity; g is the gravitational acceleration; D is the local water depth; and n is Manning's roughness, which is assumed to be uniform in the entire computational domain since no detailed roughness data was available at FIA. The 2D surface flow model is solved by a staggered leapfrog scheme [15].

Since the soil is assumed to be always close to saturation in the study area, the rainfall loss was neglected. Rainfall fall on the catchment is thus used as the effective rain intensity to generate runoff. Along the shoreline boundary, the discharge rate from the land to the sea, Q_o, was determined by the following equation,

$$Q_o = Cwh_1\sqrt{2gh_1}, \quad \ldots\ldots\ldots\ldots \quad (6)$$

where w is the width of the grid size; C is the weir coefficient ($C = 0.35$); and h_1 is the inundation depth on the land. This study did not account for flooding from the sea.

Following the estimated annual daily maximum rainfall for different return periods in the study area, this study applied 20 rainfall scenarios to investigate the flooding behavior at FIA (**Table 3**). This study simply applied a constant rainfall over a duration of either 6 hours or 12 hours. The intensity of the constant rainfall was obtained by dividing the daily rainfall by the specified duration time, 6 hours or 12 hours. This rainfall was applied uniformly over the entire computation domain. The shorter duration time, 6 hours, therefore, has a rainfall rate twice that of the longer duration time, 12 hours. The uniform rainfall was applied from the beginning of the computation for 6 or 12 hours with a computational time step of 0.5 s. The entire computation time was set to 24 hours regardless of the duration time of the rainfall so that the flooding behavior after the rainfall ceased could be observed.

4.2. Flooding Behaviors

Figure 9 shows the distributions of inundation depth at different times T after the initiation of the rainfall in rainfall case 1, in which uniform rainfall was applied from $T = 0$ to $T = 6$ hours. This study focuses on the flooding behavior at FIA, and thus the following analysis is conducted in the rectangular domain shown in **Fig. 9(d)**.

In the study area, the flooded water rapidly propagated to the regions with lower ground level. Two taxiways with relatively higher ground elevation separated the inundated region into three parts. In the following discussions, these three parts are referred to as catchments A, B, and C from west to east. The inundation stretch of the catchment A was expanded to 400 m westward from taxiway 1. A part of the runway is already inundated after just 1 hour of rainfall, that is, $T = 1$ hour (**Fig. 9(a)**). The maximum inundation depth (MID) of catchments A and C was 0.7 m, while it was 0.4 m for catchment B in **Fig. 9(a)**.

As T increases from 1 hour to 3 hours, the inundation depths and areas in A, B, and C also increased (**Fig. 9(b)**). A part of taxiway 2 was also inundated by the water from catchment C. Inundation water at some places started to flow northward over the runway, and finally spilled out to sea. Therefore, the area and the depth of inundation at $T = 3$ hours and 6 hours are about the same (**Figs. 9(b)** and **(c)**). The modeled inundation extent agreed well with that witnessed by the local staff of the airport, as shown in **Fig. 4**, while there are no measured data to validate the inundation depth.

After $T = 6$ hours, the rainfall was stopped in computation case 1. **Fig. 9(d)**, with $T = 24$ hours, shows the distribution of inundation depth at 18 hours after the stop of the rainfall. As seen in this figure, the inundation area in catchment A was significantly decreased because the inundated water flowed over the runway into the sea, while that in catchments B and C showed little change. The final inundation depth of catchment A was much larger than that of catchments B and C, indicating the importance of the drainage system for the area B and C.

Figure 3 shows the difference of MID between the heaviest rainfall event (case 15) and the weakest rainfall event (case 6). The small differences in areas B and C indicate that the water level in these areas was limited by the ground elevation of the runway on the northern side, and the excess rainfall water flowed over the runway and was discharged to the sea. On the other hand, the relatively larger difference in catchment A indicates that some water was drained before the water level reached the elevation of the runway, and thus the maximum water level was determined by the balance of the rainfall and the discharge rate through the drainage system.

5. Development of the Drainage System

As the inundation region is divided by the two taxiways into three parts, a separate drainage network must be constructed for each catchment. The present study simply ap-

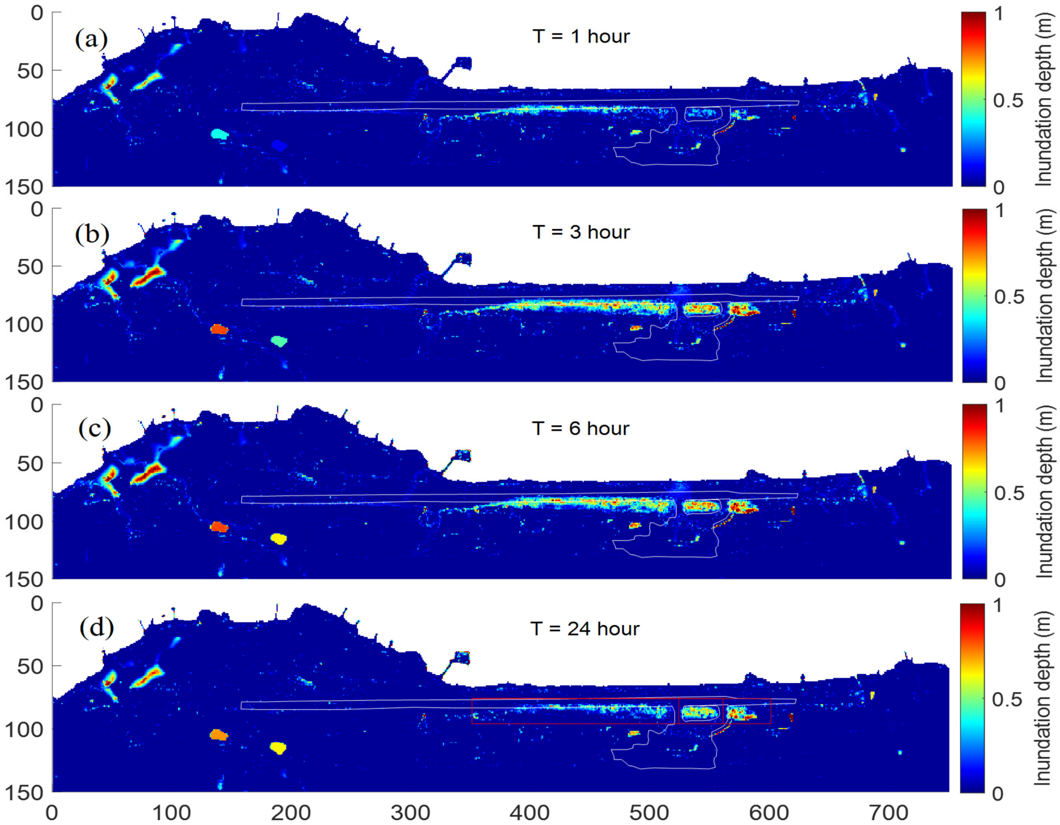

Fig. 9. Distributions of inundation depth at different times of Case 1. White line indicates the outline of the main runway, two taxiways and the terminal building. Rectangles show the target area of analysis in the following sections, called catchment A, catchment B, and catchment C, from left to right.

plied one straight underground drainage pipeline for each catchment (**Fig. 2**). The drainage pipes are assumed to be box culverts with bottom elevation fixed to 2.0 m below the mean sea level. The tops of the pipes are assumed to be equivalent to the ground elevation covered by a slotted drain; thus, surface water is directly discharged to the pipe. The origin of each pipe is located on the lowest elevation of each catchment and passes underneath the runway to the coast. Water flow in these drainage pipes was computed as one-dimensional (1D) open channel flow. The governing equations of the flow dynamics in the drainage pipes are based on the 1D Saint-Venant equations,

$$\frac{\partial Q}{\partial x}+\frac{\partial A}{\partial t}=q, \quad (7)$$

$$\frac{\partial Q}{\partial t}+\frac{\partial}{\partial x}\left(\frac{Q^2}{A}\right)+gA\frac{\partial h}{\partial x}-gA\left(S_0-S_f\right)=0, \quad (8)$$

where Q is the flow discharge positive in the seaward direction (x-direction); A is the cross-sectional area of the pipe flow; q is the flow rate from tributaries; h is the local water depth along the pipeline; S_0 is the bed slope; and S_f is the friction slope. In this study, the bottom of the pipe is horizontal so that $S_0=0$, and Manning's roughness n was applied for the estimation of S_f, i.e., $S_f=n^2Q|Q|/(A^2R^{4/3})$, where R is the hydraulic radius. The grid size in the x-direction is set equal to that of the 2D overland flow model. An explicit finite volume scheme was applied to numerically compute the 1D Saint-Venant equations with downstream boundary conditions given by the sea level. The 1D drainage pipe flow model and 2D overland flow model are computed in parallel with the same time step. At each time step, the inundation water above the drainage pipe is drained to the corresponding grid of the 1D drainage pipe flow. The discharge of surface flow to the drainage pipe is calculated by Eq. (6) if the water level in the pipe is lower than that on the corresponding land surface. The same amount of water was then reduced from the inundated water through the continuity Eq. (3) of the 2D inundation model.

Since the overall performance of the present simple drainage system should be affected by the cross-sectional area of the pipeline and by the sea water level, this study adopted different pipe widths of 0.5 m, 1.0 m, and 2.0 m and sea levels of 0.0 m, 1.5 m, and 3.0 m, respectively. Here the sea level of 1.5 m is the high tide level based on the database of Australian National Tidal Centre data for Samoa [16]. The sea level of 3.0 m accounts for the influence of future sea level rise and sea level anomaly induced by stormy waves [17]. The coupled model is simulated based on the combinations of different pipe widths and sea levels under the aforementioned rainfall scenario to investigate the flooding mitigation effect.

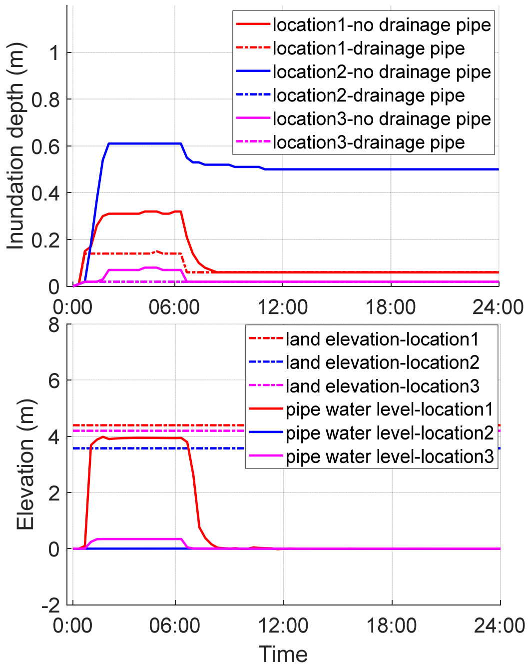

Fig. 10. Time series of inundation depths at three locations for rainfall case 1 (upper panel) and variations in water level in the corresponding grids of the drainage pipes (lower panel). Width of the drainage pipes is 0.5 m and sea level is 0 m. Locations are indicated in **Fig. 2(b)**.

5.1. Effect of Drainage Pipes on Flood Mitigation

The top panel of **Fig. 10** shows the time series of the inundation depth at three locations in each catchment near the pipeline. These locations are shown by dots in **Fig. 2(b)**. In **Fig. 10**, dashed and solid lines indicate the computed results with and without the drainage pipelines, respectively. The bottom panel of **Fig. 10** shows the time series of the water level inside the drainage pipe in the vicinity of locations 1, 2, and 3. It is obvious that the installation of drainage pipes greatly reduces the inundated water depth. Besides the peak water depth, the duration time of the peak inundation was also reduced by the drainage pipes. In all cases, the inundation water depth rapidly increases with time and then reaches a nearly constant peak depth. This equilibrium state should be achieved when the total amount of rainfall in each catchment becomes equivalent to the water discharge from each catchment. In the case of no drainage, this constant peak depth corresponds to the elevation of the nearby runway since water higher than the runway is discharged to the sea. In the case with a drainage pipe, equilibrium water depth is determined by the balance between rainfall and the discharge rate to the drainage system. As seen in the bottom panel of **Fig. 10**, the water level in the pipe at locations 2 and 3, corresponding to catchments B and C, is clearly lower than the ground level. The discharge rate from the ground to the drainage pipe is therefore determined only by the inundation water depth around the pipe but not by the water level in the pipe. On the other hand, the water level in the pipe at location 1, corresponding to catchment A, is nearly as high as the bed level. The discharge rate in catchment A is thus affected both by the inundation water depth and by the instantaneous water level inside the drainage pipe.

Figures 11(a) and **(b)** show the distribution of MID of rainfall of case 15 without and with the drainage pipes, respectively. **Fig. 11(c)** shows the difference in MID between the cases with and without drainage pipes. Drainage pipes significantly reduced MID and successfully avoided the inundation of the two taxiways. This result indicates that a single drainage pipe with a width of 2 m was adequate to protect catchments B and C from flooding even under future rainfall with a return period of 125 years. On the other hand, part of the runway was still flooded in catchment A even with the drainage pipeline. An additional drainage system may be needed to protect catchment area A since it is larger than B and C.

5.2. Sensitivity Analysis of Flood Mitigation Effects of Different Pipe Widths and Sea Levels

This section investigates the sensitivity of the effectiveness of the drainage pipelines to the width of pipelines and the sea water level, respectively. To evaluate the overall effectiveness of the drainage system in each case, the spatially averaged MID was computed in each catchment area, A, B, and C. Hereafter, this paper defines MID as the horizontally averaged local maximum inundation depth in each catchment. **Fig. 12** shows the MID in each catchment under different rainfall and pipe width conditions. In the figure, the horizontal axis indicates the rainfall intensity (mm/h); 6-hour-rainfall is indicated by filled markers and 12-hour-rainfall is indicated by unfilled markers. The duration time of the rainfall shows little effect on MID since MID rapidly reaches the equilibrium state, as seen in **Fig. 10**. With installation of drainage pipes, MID was significantly decreased in all of the catchments. In catchment A, MID was reduced by 0.8 m by a drainage pipe with a width of 0.5 m. The pipe with a width of 1.0 m further reduced the water depth. However, the difference in MID between the cases of 1 m-wide and 2 m-wide pipes was relatively small, suggesting that a pipe width of 1.0 m is adequate to discharge the rainfall when the rainfall intensity is not significantly high. In the case of catchments B and C, there is little difference in MID by the width of the drainage pipe. This result indicates that 0.5 m-wide pipe is sufficient for flood mitigation in catchments B and C.

Similarly, **Fig. 13** shows the result for MID under different conditions of rainfall and sea water level. Elevated sea level reduces the water level gradient and thus reduces the discharge flow rate through the drainage pipe. It is found that the computed MID showed little difference within the range of astronomical tide level, 0, 0.75, and 1.5 m. The difference of MID was around 0.003 m within this tide range at catchment A. This difference was much smaller for the other two catchments, B and C. As discussed previously, the flow discharge through the drainage pipe is sufficiently larger than the drainage flow

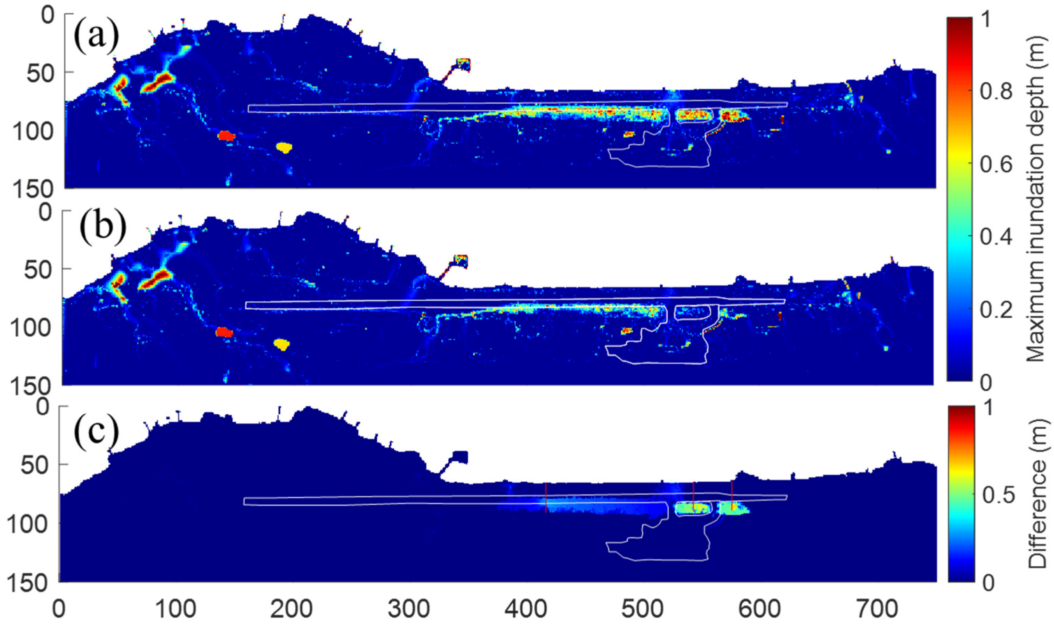

Fig. 11. Distribution of MID of rainfall Case 15. (a) Without drainage pipe; (b) with drainage pipe, pipe width = 2.0 m, sea level = 1.5 m; (c) difference in MID between (a) and (b).

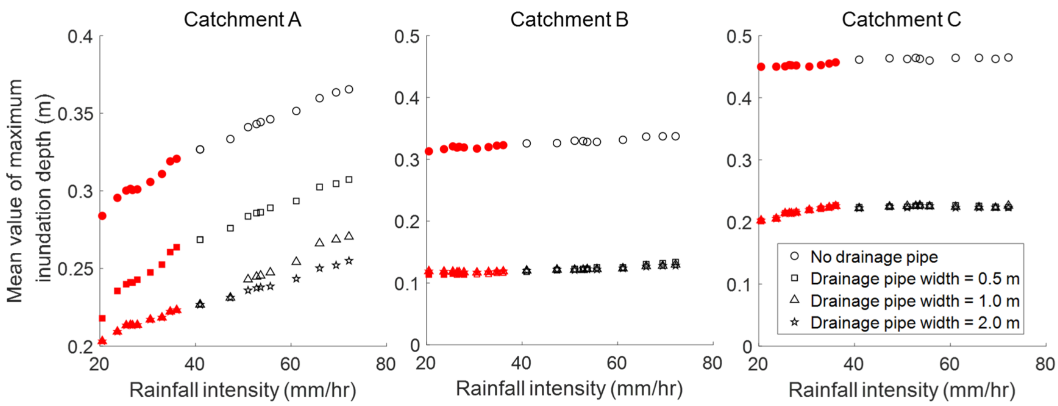

Fig. 12. Sensitivity analysis of the impact of drainage pipe width on flood mitigation effect. Sea level is set at 0 m. 6-hour-rainfall is indicated by filled markers and 12-hour-rainfall is indicated by unfilled markers.

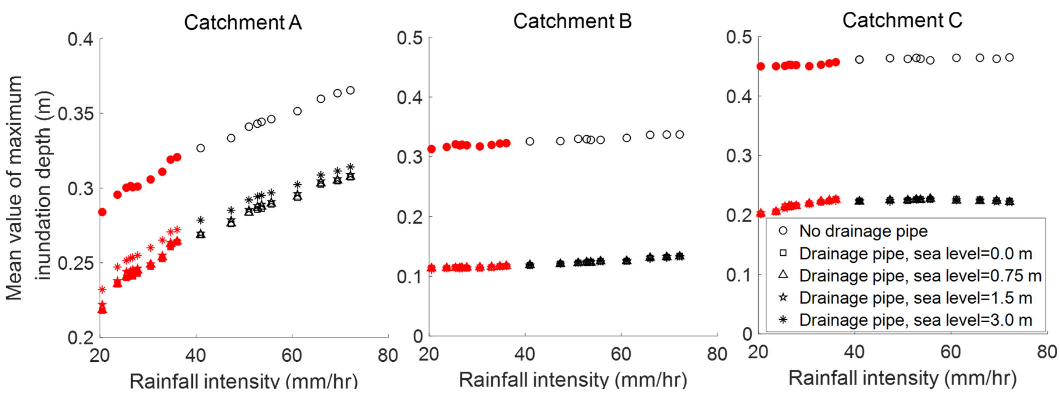

Fig. 13. Sensitivity analysis of the impact of sea level on flood mitigation effect. Drainage pipe width is set at 0.5 m. 6-hour-rainfall is indicated by filled markers and 12-hour-rainfall is indicated by unfilled markers.

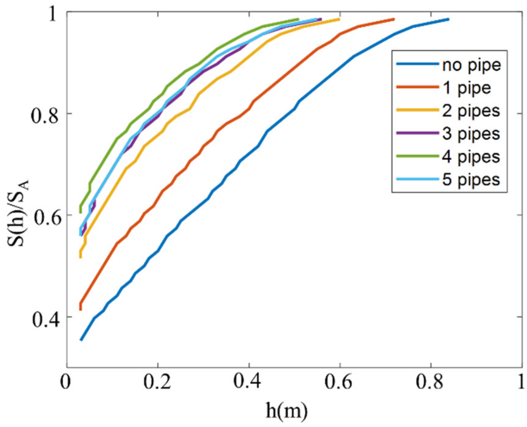

Fig. 14. Rate of inundation area of catchment A as a function of inundation depth with installation of multiple drainage pipes.

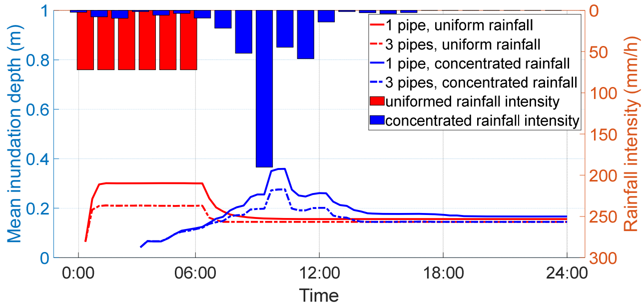

Fig. 15. Comparison of variations in mean inundation depth at catchment A between a uniform and a concentrated rainfall event.

rate from the ground to the pipe. The reduction of the flow rate due to the increase of the sea level therefore had no influence on MID, especially in catchments B and C. On the other hand, a clear increase of MID was observed at catchment A when the sea level is 3.0 m, under the assumption of future sea level rise with a certain sea level anomaly due to stormy waves and surges. The influence of future sea level therefore may be accounted for in the future drainage system.

6. Discussion

As shown in the previous section, a single drainage pipe with a relatively small width was adequate to mitigate the flood risk for catchments B and C. However, multiple drainage pipes may be needed for flood prevention in catchment A. While the larger width of a drainage pipe increases the potential discharge rate of the pipe, the results shown in **Fig. 12** indicate that the effectiveness of wider pipelines is limited because the discharge rate from the ground surface to the pipeline becomes independent of the width of the pipeline if the water level inside the pipeline is lower than ground level. Multiple drainage pipes, therefore, may have a better effect on efficient drainage for flood prevention in catchment A. **Fig. 14** illustrates the rate of $S(h)$ and S_A as functions of the inundation depth, h, and the number of pipelines, N. Here S_A is the total area of the catchment A and $S(h)$ is the area with a local MID lower than h. In this manner, one can see the distribution of the local maximum water depth in the entire catchment area, A. The number of drainage pipes, N, was varied from $N = 0$ to $N = 5$. The drainage pipes were placed at equal alongshore intervals within the entire stretch of catchment A. The sea level and the pipe width were set to 1.5 m and 2.0 m, respectively. Rainfall scenario case 15 was used in all the numerical experiments. As seen in the figure, the amount of inundated area with higher inundation significantly decreases with the number of pipelines, N. It should, however, be noted that a clear effect of increasing N can be seen up to $N = 3$, and the computed results are nearly the same when N is 3, 4, and 5. It should also be noted that the decrease of inundation depth in the case of $N = 4$ was slightly better than that of $N = 5$. This indicates the importance of the location of the drainage pipes. The drainage pipe should be placed at an area with relatively lower ground level where the flooding water tends to concentrate.

This study applied a constant rainfall over the duration time of 6 or 12 hours. In reality, however, there should be a certain time variation in the rainfall intensity. The daily rainfall may be more concentrated, resulting in a much higher intensity. **Fig. 15** illustrates the time series of mean inundation depth of catchment A based on a uniform and concentrated rainfall. These two scenarios have the same daily rainfall amount. It is found that the mean value of MID of the concentrated rainfall scenario is larger than that of the uniform rainfall, suggesting that torrential rainfall with very high intensity may require more powerful drainage networks to prevent the inundation of the runway.

7. Conclusions

This paper investigated the inland flooding behavior around Faleolo International Airport, Samoa, and explored probable drainage strategies by considering future climate change. High-spatial resolution future rainfall information (HRFR) was estimated using satellite-based rainfall data and future projections by GCMs. Then, annual maximum daily rainfalls for different return periods were estimated for the present and future climate. Results showed that maximum daily rainfall could reach 245.8 mm and 432.7 mm with a return period of 125 years under the present and future climate condition, respectively. This study applied a new method for estimation of the future rainfall. More detailed validation of the proposed new method through comparisons with observed data is left for future tasks. Moreover, this study applied single GCM projection. Application of multiple GCM projections is necessary to take into consideration the uncertainties of climate change.

The estimated daily rainfall was used as forcing in a 2D overland flow model to estimate the flooding behavior around the study area. It was found that the flooding mainly occurs to the south of the runway. The flooding area is separated by the two taxiways into three parts. The mean value of the MID generally increases with the rainfall intensity, and parts of the runway may be inundated under heavy rainfall.

Three drainage pipes were placed in the flooding area to discharge the rainfall water to the coast. Sensitivity analysis was conducted to investigate the flood mitigation effect of the drainage system for different sea levels and pipe widths. The results showed that a single drainage pipe is adequate to prevent severe inundation in catchments B and C, while multiple drainage pipes are necessary for catchment A. Compared to the number and width of the pipeline, drainage capability was not very sensitive to the sea level. Little difference was observed in the drainage performance if the sea level difference was within the range of astronomical tide. Non-negligible influence, however, was observed if the water level was raised to 3 m, which could likely occur under the scenario of sea level rise and sea level anomaly due to stormy waves. Increased width of the pipeline showed a certain limited effect on drainage capability. Besides width, increases in the number of pipes also showed a clear effect of reducing inundation. The location of the drainage pipes plays an important role in effectively reducing the flooding risk. Using a larger number of drainage pipes is not always the optimum strategy for flooding mitigation. Torrential rainfall with significantly high intensity introduces much uncertainty and raises difficulties for the development of drainage strategy.

Acknowledgements

This study was conducted as a part of the project for evaluation of the impact of climate change on coastal hazards of South Pacific Islands supported by the Ministry of the Environment, Japan. A part of this study was also conducted as a research activity of "Enhancement of National Resilience against Natural Disasters" of the Cross-ministerial Strategic Innovation Promotion Program (SIP), under the supervision of NIED. The program was supported by the Council for Science, Technology and Innovation (CSTI).

References:

[1] The Core Writing Team, R. K. Pachauri and L. A. Meyer (Eds.), "Climate Change 2014: Synthesis Report. Contribution of Working Groups I, II and III to the Fifth Assessment Report of the Intergovernmental Panel on Climate Change," Intergovernmental Panel on Climate Change (IPCC), 151pp., 2014.

[2] J. Barnett and J. Campbell, "Climate Change and Small Island States: Power, Knowledge and the South Pacific," Earthscan, 2010.

[3] C. Farbotko and H. Lazrus, "The first climate refugees? Contesting global narratives of climate change in Tuvalu," Global Environmental Change, Vol.22, No.2, pp. 382-390, doi: 10.1016/j.gloenvcha.2011.11.014, 2012.

[4] V. Gornitz, "Global coastal hazards from future sea level rise," Global and Planetary Change, Vol.3, Issue 4, pp. 379-398, doi: 10.1016/0921-8181(91)90118-G, 1991.

[5] A. Toimil, P. Camus, I. J. Losada, G. Le Cozannet, R. J. Nicholls, D. Idier, and A. Maspataud, "Climate change-driven coastal erosion modelling in temperate sandy beaches: Methods and uncertainty treatment," Earth-Science Reviews, Vol.202, Article No.103110, doi: 10.1016/j.earscirev.2020.103110, 2020.

[6] K. Ng, P. Borges, M. R. Phillips, A. Medeiros, and H. Calado, "An integrated coastal vulnerability approach to small islands: The Azores case," Science of the Total Environment, Vol.690, pp. 1218-1227, doi: 10.1016/j.scitotenv.2019.07.013, 2019.

[7] K. Trenberth, "Changes in precipitation with climate change," Climate Research, Vol.47, Nos.1-2, pp. 123-138, doi: 10.3354/cr00953, 2011.

[8] W. K. Michener, E. R. Blood, K. L. Bildstein, M. M. Brinson, and L. R. Gardner, "Climate Change, Hurricanes and Tropical Storms, and Rising Sea Level in Coastal Wetlands," Ecological Applications, Vol.7, Issue 3, pp. 770-801, doi: 10.2307/2269434, 1997.

[9] K. Walsh and A. B. Pittock, "Potential Changes in Tropical Storms, Hurricanes, and Extreme Rainfall Events as a Result of Climate Change," Climatic Change, Vol.39, Issue 2, pp. 199-213, doi: 10.1023/A:1005387120972, 1998.

[10] T. Kubota, K. Aonashi, T. Ushio, S. Shige, Y. N. Takayabu, M. Kachi, Y. Arai, T. Tashima, T. Masaki, N. Kawamoto, T. Mega, M. K. Yamamoto, A. Hamada, M. Yamaji, G. Liu, and R. Oki, "Global Satellite Mapping of Precipitation (GSMaP) Products in the GPM Era," V. Levizzani, C. Kidd, D. B. Kirschbaum, C. D. Kummerow, K. Nakamura, and F. J. Turk (Eds.), "Satellite Precipitation Measurement: Volume 1," pp. 355-373, Springer, doi: 10.1007/978-3-030-24568-9_20, 2020.

[11] K. E. Taylor, R. J. Stouffer, and G. A. Meehl, "An Overview of CMIP5 and the Experiment Design," Bulletin of the American Meteorological Society, Vol.93, Issue 4, pp. 485-498, doi: 10.1175/BAMS-D-11-00094.1, 2012.

[12] T. Iizumi, M. Nishimori, Y. Ishigooka, and M. Yokozawa, "Introduction to climate change scenario derived by statistical downscaling," J. of Agricultural Meteorology, Vol.66, No.2, pp. 131-143, doi: 10.2480/agrmet.66.2.5, 2010 (in Japanese with English abstract).

[13] T. Iizumi, M. Nishimori, K. Dairaku, S. A. Adachi, and M. Yokozawa, "Evaluation and intercomparison of downscaled daily precipitation indices over Japan in present-day climate: Strengths and weaknesses of dynamical and bias-correction-type statistical downscaling methods," J. of Geophysical Research: Atmospheres, Vol.116, Issue D1, doi: 10.1029/2010JD014513, 2011.

[14] AW3D Enhanced, https://www.aw3d.jp/en/products/enhanced/ [accessed January 6, 2021]

[15] C. K. Birdsall and A. B. Langdon, "Plasma Physics via Computer Simulation," McGraw-Hill, 1984.

[16] Permanent Service for Mean Sea Level, https://www.psmsl.org/data/obtaining/stations/1840.php [accessed January 6, 2021]

[17] Y. Tajima, T. Shoji, and K. Taniguchi, "Study on Probabilistic Inundation Hazard along the Coast of South Pacific Islands: Case study at Lakeba Island in Fiji," J. of Japan Society of Civil Engineers Ser. B2 (Coastal Engineering), Vol.76, No.2, pp. I_1231-I_1236, doi: 10.2208/kaigan.76.2_I_1231, 2020.

Name:
Lianhui Wu

Affiliation:
Project Researcher, Department of Civil Engineering, The University of Tokyo

Address:
7-3-1 Hongo, Bunkyo-ku, Tokyo 113-8656, Japan

Brief Career:
2017- Project Researcher, Department of Civil Engineering, The University of Tokyo

Selected Publications:
- "Study on characteristics of SAR imagery around the coast for shoreline detection," Coastal Engineering J., Vol.61, Issue 2, pp. 152-170, doi: 10.1080/21664250.2018.1560685, 2018.

Academic Societies & Scientific Organizations:
- Japan Society of Civil Engineers (JSCE)

Name:
Kenji Taniguchi

Affiliation:
Associate Professor, School of Geosciences and Civil Engineering, Kanazawa University

Address:
Kakuma-machi, Kanazawa, Ishikawa 920-1192, Japan

Brief Career:
2005- The University of Tokyo
2008- Kanazawa University

Selected Publications:
• "A Simple Ensemble Simulation Technique for Assessment of Future Variations in Specific High-Impact Weather Events," J. of Geophysical Research: Atmosphere, Vol.123, Issue 7, pp. 3443-3461, doi: 10.1002/2017JD027928, 2018.
• "Variations in Extreme Wave Events near a South Pacific Island under Global Warming: Case Study of Tropical Cyclone Tomas," Progress in Earth and Planetary Science, Vol.7, Issue 1, Article No.8, doi: 10.1186/s40645-020-0321-y, 2020.

Academic Societies & Scientific Organizations:
• Japan Society of Civil Engineers (JSCE)
• Meteorological Society of Japan (MSJ)
• Japan Society of Hydrology and Water Resources (JSHWR)
• American Geophysical Union (AGU)

Name:
Yoshimitsu Tajima

Affiliation:
Professor, Department of Civil Engineering, The University of Tokyo

Address:
7-3-1 Hongo, Bunkyo-ku, Tokyo 113-8656, Japan

Brief Career:
1996-2005 Penta-Ocean Construction Co., Ltd.
2005-2007 Assistant Professor, The University of Tokyo
2007-2013 Associate Professor, The University of Tokyo
2013- Professor, The University of Tokyo

Selected Publications:
• "Study on shoreline monitoring system based on satellite SAR imagery," Coastal Engineering J., Vol.61, Issue 3, pp. 401-421, doi: 10.1080/21664250.2019.1619252, 2019.
• "Numerical modeling of ship wave generation using Green's functions based on linear dispersive wave theory," Coastal Engineering J., Vol.62, Issue 2, pp. 317-335, doi: 10.1080/21664250.2020.1755794, 2020.

Academic Societies & Scientific Organizations:
• Japan Society of Civil Engineers (JSCE)